The Astrophysical Journal, 713:959–969, 2010 April 20 doi:10.1088/0004-637X/713/2/959

PROPERTIES OF GALACTIC CIRRUS CLOUDS OBSERVED BY BOOMERANG

M. Veneziani[1,2], P. A. R. Ade[3], J. J. Bock[4,5], A. Boscaleri[6], B. P. Crill[4,5], P. de Bernardis[1], G. De Gasperis[7], A. de Oliveira-Costa[8], G. De Troia[7], G. Di Stefano[9], K. M. Ganga[2], W. C. Jones[10], T. S. Kisner[11], A. E. Lange[4], C. J. MacTavish[12], S. Masi[1], P. D. Mauskopf[3], T. E. Montroy[11], P. Natoli[7], C. B. Netterfield[13], E. Pascale[13], F. Piacentini[1], D. Pietrobon[7,14], G. Polenta[1,15,16], S. Ricciardi[1,17], G. Romeo[9], and J. E. Ruhl[11]

[1] Dipartimento di Fisica, Università di Roma "La Sapienza," Rome, Italy; marcella.veneziani@roma1.infn.it
[2] APC, Université Paris Diderot, 75013 Paris, France
[3] Department of Physics and Astronomy, Cardiff University, Cardiff, UK
[4] Jet Propulsion Laboratory, Pasadena, CA 91109, USA
[5] California Institute of Technology, Pasadena, CA 91125, USA
[6] IFAC-CNR, 50127, Firenze, Italy
[7] Dipartimento di Fisica, Università di Roma "Tor Vergata," Rome, Italy
[8] Department of Physics, MIT, Cambridge, MA 02139, USA
[9] Istituto Nazionale di Geofisica e Vulcanologia, 00143 Rome, Italy
[10] Department of Physics, Princeton University, Princeton, NJ 08544
[11] Case Western Reserve University, Cleveland, OH 44106, USA
[12] Astrophysics Group, Imperial College, London, UK
[13] Physics Department, University of Toronto, Toronto, ON, Canada
[14] Institute of Cosmology and Gravitation, University of Portsmouth, UK
[15] ASI Science Data Center, c/o ESRIN, 00044 Frascati, Italy
[16] INAF-Osservatorio Astronomico di Roma, I-00040 Monte Porzio Catone, Italy
[17] Computational Research Division, LBNL, Berkeley, CA 94720, USA

Received 2009 July 28; accepted 2010 March 1; published 2010 March 29

ABSTRACT

The physical properties of galactic cirrus emission are not well characterized. BOOMERANG is a balloon-borne experiment designed to study the cosmic microwave background at high angular resolution in the millimeter range. The BOOMERANG 245 and 345 GHz channels are sensitive to interstellar signals, in a spectral range intermediate between FIR and microwave frequencies. We look for physical characteristics of cirrus structures in a region at high galactic latitudes ($b \sim -40^\circ$) where BOOMERANG performed its deepest integration, combining the BOOMERANG data with other available data sets at different wavelengths. We have detected eight emission patches in the 345 GHz map, consistent with cirrus dust in the *Infrared Astronomical Satellite* maps. The analysis technique we have developed allows us to identify the location and the shape of cirrus clouds, and to extract the flux from observations with different instruments at different wavelengths and angular resolutions. We study the integrated flux emitted from these cirrus clouds using data from *Infrared Astronomical Satellite* (*IRAS*), DIRBE, BOOMERANG and *Wilkinson Microwave Anisotropy Probe* in the frequency range 23–3000 GHz (13 mm–100 μm wavelength). We fit the measured spectral energy distributions with a combination of a gray body and a power-law spectra considering two models for the thermal emission. The temperature of the thermal dust component varies in the 7–20 K range and its emissivity spectral index is in the 1–5 range. We identified a physical relation between temperature and spectral index as had been proposed in previous works. This technique can be proficiently used for the forthcoming Planck and Herschel missions data.

Key words: cosmology: observations – ISM: clouds – radio continuum: ISM – submillimeter: ISM

Online-only material: color figures

1. INTRODUCTION

Characterizing the properties of dust in our Galaxy is an important topic of millimeter (mm) and submillimeter astrophysical observations. At frequencies above 100 GHz this emission is dominated by thermal radiation from large grains in equilibrium with the interstellar radiation field. Interstellar dust is distributed in filamentary cirrus-like clouds and covers the sky at both low and high galactic latitudes (Low et al. 1984). This emission is usually described by a thermal spectrum, parameterized by the physical temperature of the grains T_d and by their emissivity versus frequency, which is assumed to be a power law with spectral index β. While dust properties have been deeply studied in the galactic plane (Désert et al. 2008; Dupac et al. 2003; Lagache et al. 1998), there is a little information at high galactic latitudes (Arendt et al. 1998; Boulanger et al. 1996; Kiss et al. 2006; Bot et al. 2009; Pascale et al. 2008).[18] Dust emission at high galactic latitudes is interesting for two reasons. First, at these latitudes the detection of each structure is very little affected by the overlap of other structures along the line of sight; this allows an unequivocal estimation of the physical properties of the observed cloud. Second, a good knowledge of dust emission at high galactic latitudes is crucial to determine its potential contamination of the cosmic microwave background (CMB) measurements, and to improve component separation techniques (Leach et al. 2008).

In the mm range there is a lack of observational data, and different models have been proposed by Finkbeiner et al. (1999,

[18] Knowledge of dust properties has been improved recently by the BLAST experiment (see Pascale et al. 2008; Netterfield et al. 2009, and references therein).

FDS hereafter) to extrapolate the data measured by the *IRAS* (Neugebauer et al. 1984) to the microwave frequency range.

BOOMERanG-03 offers an unprecedented combination of coverage and sensitivity, providing $\sim 10^\circ \times 10^\circ$ maps of a high latitude region centered at $b \sim -40^\circ$, at 145, 245, and 345 GHz, with an angular resolution $\lesssim 10'$. This instrument derives directly from the BOOMERanG payload flown in 1997/1998. That payload was recovered and modified to make it sensitive to polarization and to improve the hardware, keeping almost the same spectral coverage and angular resolution. For further information on the BOOMERanG-98 instrument see Crill et al. (2003), and previous results on interstellar dust detected by BOOMERanG-98 at high galactic latitudes are reported in Masi et al. (2001).

In this paper, we present an analysis of the characteristics of diffuse dust emission from far-infrared (FIR) to microwave frequencies in the nearby interstellar medium, at galactic latitudes $-50^\circ < b < -15^\circ$, using the BOOMERanG03 (Masi et al. 2006), *Wilkinson Microwave Anisotropy Probe* (*WMAP*; Hinshaw et al. 2007), *IRAS* (Neugebauer et al. 1984), and Diffuse Infra-Red Background Experiment (DIRBE; Boggess et al. 1992) data. In particular, we focus on the observation of eight high-latitude cirrus clouds located in the BOOMERanG deep integration field. We derive physical parameters of the dust in the clouds, and we study the relation between these parameters which can provide insight into the nature of the dust grains as suggested by Meny et al. (2007).

The paper is structured as follows. Section 2 describes the data sets and the calibration; Section 3 describes the pipeline adopted; Section 4 reports the results on the dust properties. Conclusions are discussed in Section 5.

2. DATA PROCESSING

BOOMERanG03 (hereafter B03) is a balloon-borne experiment which in 2003 January performed a 14 day flight over Antarctica. It can be considered a pathfinder for the High Frequency Instrument of the *Planck* satellite since it validated the detectors, the scanning strategy, and initiated the relevant data analysis techniques. B03 has observed the microwave sky in three frequency bands centered at 145, 245, and 345 GHz with high angular resolution ($\sim 10'$ at 145 GHz, $\sim 7'$ at 245 and 345 GHz). While the 145 GHz channel is devoted to CMB studies, the two high frequency channels mainly monitor foreground emission. The observed region covers approximately 4% of the sky in the southern hemisphere and has been divided in three areas: a "deep" (long integration) survey of ~ 90 deg^2, a "shallow survey" region of ~ 750 deg^2 and a region of ~ 300 deg^2 across the galactic plane. A detailed description of the B03 instrument and scanning strategy is published in Masi et al. (2006).

In this work, we study the dust properties by analyzing the 245 and 345 GHz channel observations in the deep region ($70^\circ <$ R.A. $< 95^\circ$ and $-52^\circ <$ decl. $< -39^\circ$), which provides high signal-to-noise ratio observations of interstellar dust emission at high galactic latitudes. B03 bands are in a particularly key position for the study of interstellar dust because they cover the Rayleigh–Jeans part of its spectrum, which is currently poorly constrained by observations, and they allow us to test the extrapolation of the models to long wavelengths (Finkbeiner et al. 1999).

In the 245 and 345 GHz detectors, radiation is concentrated on spider web bolometers by cold horn assemblies. A metal wire grid is placed in front of each detector, so that it is sensitive only to one of the two orthogonal polarizations. Intensity and polarization measurements can be derived combining signals from different detectors. In this paper, we focus on the temperature signal only. Previous B03 results on CMB and foregrounds are described in Jones et al. (2006), Piacentini et al. (2006), Montroy et al. (2006), MacTavish et al. (2006), De Troia et al. (2007), Natoli et al. (2009), and Veneziani et al. (2009).

In order to study the physical properties of diffuse dust over a wide range of frequencies, we include in our analysis the *IRAS* data sets at 100 μm (I100 in the following), the DIRBE data set at 240 μm (D240 in the following), and the five 5 yr *WMAP* bands[19] *K*, *Ka*, *Q*, *V*, and *W*, centered at 23, 33, 41, 61, and 93 GHz, respectively. For the *IRAS* data, we use the Improved Reprocessing of the *IRAS* Survey[20] described in Miville-Deschênes & Lagache (2005).

2.1. Timeline Processing and Cosmic Microwave Background Removal

The 245 and 345 GHz channels of B03 (hereafter B245 and B345, respectively) have four bolometers each, named W, X, Y, and Z. In this analysis, we consider only bolometers W, Y, and Z at 245 GHz and W, X, and Y at 345 GHz—the other detectors were affected by anomalous instrumental noise (Masi et al. 2006).

As in the standard pipeline, the raw time-ordered data (TOD) from each detector is deconvolved from its transfer function to remove the filtering effects of the readout electronics and of the time response of the detectors. The pointing is recovered from on-board attitude sensors, and bad data are flagged and not used for the analysis. The deconvolved time lines are then reduced with the ROMA map-making code (de Gasperis et al. 2005) to produce brightness maps using the Healpix[21] scheme (Górski et al. 2005). Since we are looking for large-scale structures, we use a pixel size of $13\farcm7$ (which corresponds to $N_{\rm side} = 256$) in this analysis.

At the frequency range and the observed region of the BOOMERanG experiment, the dust signal can sometimes be comparable/subdominant to the measured CMB anisotropy. Therefore, to study the physical properties of the diffuse dust at the BOOMERanG data, we need first to remove the CMB signal from the 245 and the 345 GHz maps before performing any foreground studies on these data. In order to remove the CMB signal, we operated as follows:

1. Since at 145 GHz dust emission is subdominant with respect to CMB anisotropy (Masi et al. 2006), we calibrate the BOOMERanG 245 and 345 GHz data using the *WMAP* and the BOOMERanG-98 data. In harmonic space, we compute the slope of the linear correlation between the BOOMERanG 245 (345) GHz map and the BOOMERanG-98 150 GHz map, and the slope of the linear correlation between the *WMAP*-94 GHz map and the BOOMERanG-98 150 GHz map. The ratio of the two slopes is a measurement of the calibration factor (in volt/$K_{\rm CMB}$) of the 245 (345) GHz data of BOOMERanG. For example,

$$\mathcal{K}_{245X} = \frac{\langle a_{\ell m}^{245X} \times a_{\ell m}^{B98} \rangle}{\langle a_{\ell m}^{WMAP} \times a_{\ell m}^{B98} \rangle}. \quad (1)$$

[19] http://lambda.gsfc.nasa.gov
[20] http://www.cita.utoronto.ca/~mamd/IRIS/
[21] http://healpix.jpl.nasa.gov

In other words, we calibrate our detectors with respect to *WMAP*, using the B98 map as a transfer to select only the CMB part of the map. To account for different beams and scanning strategy, each $a_{\ell m}$ has been previously divided by its window function as discussed in Masi et al. (2006). The calibration factors on CMB against the reference channels B245W and B345W are reported in second column of Table 1.

2. We remove the CMB dipole signal from the time lines using a template derived from the parameters given in Mather et al. (1994). Then we subtract the 145 GHz map from the 245 and 345 GHz CMB calibrated time lines.
3. The CMB subtracted time lines are combined into a single detector map using the ROMA iterative map-making code (de Gasperis et al. 2005). The TOD is then high-pass filtered at 20 mHz to remove large-scale signal from the CMB dipole, system drifts and to correct for the non-perfect knowledge of the transfer function of detectors.
4. The relative calibration of the resulting CMB subtracted map is corrected for the effect of different spectral band-passes by using the *IRAS* 100 μm map as transfer:

$$\mathcal{R}_{245X/245W} = \frac{\left\langle a_{\ell m}^{245X} \times a_{\ell m}^{IRAS} \right\rangle}{\left\langle a_{\ell m}^{245W} \times a_{\ell m}^{IRAS} \right\rangle}. \quad (2)$$

5. These relative calibration corrections have been applied to the CMB subtracted time lines to obtain multi-detector maps, one at 245 GHz and another at 345 GHz. They are reported in third column of Table 1.

In order to take into account the effect of the BOOMERANG scanning strategy, the maps derived from the other experiments are projected onto four time streams corresponding to the four BOOMERANG photometers. The time lines are then filtered in the same way and assembled in a multi-detector map replicating the flight pointing and flagging of BOOMERANG. We correct for the slight effect of this procedure on the measured fluxes as described in Section 3.1. The CMB from the *WMAP* maps has been removed using the 145 GHz BOOMERANG channel. All our maps are thus CMB cleaned, with the assumption that the BOOMERANG 145 GHz data are CMB dominated; indeed, in Figure 33 of Masi et al. (2006) it is shown that at 145 GHz dust rms is much less than CMB rms. Nevertheless, it is possible that some residual dust flux is present in our 145 GHz map in the cirrus cloud regions. We estimated the possible dust residual using the recovered models (see Section 4) and we find that the contamination can be of the order of 5% of the signal at 345 GHz expressed in CMB temperature units. This contamination on brightness has the same value at all frequencies when expressed in CMB thermodynamic units, and we have seen that it amounts to a fraction of the error bars of the measured average brightness of the cirrus clouds at all frequencies.

3. DATA ANALYSIS

The goal of this work is the estimation of the physical properties of cirrus structures through the measurement of their flux over a wide frequency range. Thus, when measuring the flux, we need to collect all and only pixels with dust emission. Since dust emission peaks at high frequency, we choose the maps with the highest signal-to-noise ratio, B345 and I100, to select the brightest pixels belonging to dust structures. We then combined B345 and I100 in pixel space producing a correlation map given by

$$M(p) \equiv \frac{I_{B345}(p) \times I_{I100}(p)}{\sqrt{\frac{1}{N_p^2} \sum_{p'} I_{B345}^2(p') \sum_{p'} I_{I100}^2(p')}} = \frac{I_{B345}(p) \times I_{I100}(p)}{\sigma_{B345} \times \sigma_{I100}}, \quad (3)$$

where p identifies a pixel in the Healpix scheme, I is the intensity map, and σ is the rms of the intensity in the observed region. The equality in Equation (3) holds since the average of the intensity maps is vanishing because of the high-pass filtering procedure. The normalization has been chosen in such a way that the correlation between two identical maps, summed over all pixels, is 1. Since we are interested in positive emission regions only, we masked the negative emission ones when computing the correlation map.

With this procedure we could identify eight large clouds which are marked by black circles in Figure 1. As a starting point for the pixel selection, in each of these areas we select the brightest pixels by imposing a threshold $M(p) > 1.5$. This value allows us to include cold sources that have a faint signal in the I100 map. In order to preserve the irregular shape of the clouds, later on we increased the initial area in steps, extending it by 0.°1 around each pixel. We choose this step size since pixels have 0.°22 side ($N_{\rm side} = 256$), so 0.°1 starting from the center of the pixel is the minimum distance to collect another pixel. We patch a maximum distance of 1° from the starting mask, to avoid contributions from other structures. In this way, we preserve the shape of the significantly correlated region in the correlation map and include the other pixels dominated by dust emission, without missing any. The integrated flux increases and reaches a maximum; then it decreases if we further widen the selected area. In fact, the detectors are AC coupled and produce negative bounces after detecting a positive signal from a localized source. The error bars on the flux are given by adding in quadrature the errors of each pixel belonging to the mask. We use this effect to detect the area to be included in the flux measurement deriving the dimension of the mask corresponding to the maximum flux through a Gaussian fit. We then associate with each cloud the flux and the error corresponding to that mask size. The brightness maps are shown in Figure 2, and flux values and errors are reported in Table 2. An example of this technique is shown in Figure 3 and the increasing mask method is shown in Figure 4. From Figure 3 we can see that the flux does not depend strongly on the mask radius. In *WMAP Q*, *Ka*, and *K* bands the beam size is comparable to the size of the smaller cirrus clouds. In these cases we measure the flux as the integral of the brightness over a circle centered in the source coordinates,

Table 1
Relative Gains of BOOMERANG Detectors

Channel	$\mathcal{K}_{*W}$	$\mathcal{R}_{*W}$
245X	1.00 ± 0.08	1.09 ± 0.02
245Y	1.03 ± 0.07	1.15 ± 0.02
245Z	1.16 ± 0.06	1.17 ± 0.02
345X	0.85 ± 0.15	0.92 ± 0.03
345Y	1.47 ± 0.16	1.26 ± 0.02
345Z	1.23 ± 0.18	0.94 ± 0.02

Notes. BOOMERANG detectors relative gains for CMB (second column) and dust (third column) against the reference channels B245W and B345W, respectively. The comparison is done with the cross-spectra method (see the text). 1σ errors are reported.

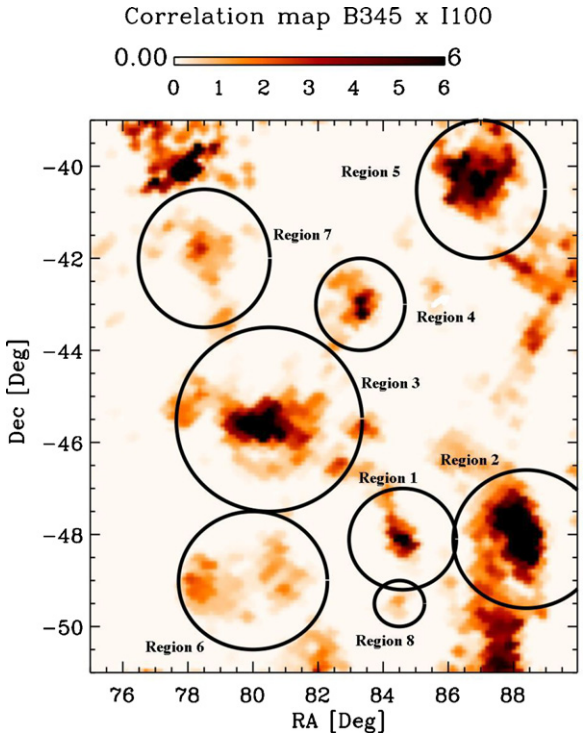

Figure 1. Correlation map (Equation (3)) between B345 and I100. All positive structures shown in the map above were included in the final mask, with the exception of the regions centered at (R.A., decl.) = (78°, −40°), and (88°, −50°) and the region 85° < R.A. < 90° and −46° < decl. < −42°. They are small parts of very complex shaped structures which have their largest part in the BOOMERANG shallow field.

(A color version of this figure is available in the online journal.)

with a $3\sigma_{\rm BEAM}$ radius. We also check that this flux is consistent with the flux measured with the method described above.

We apply this procedure for each cirrus cloud at each frequency taking into account the noise and beam characteristics of each experiment. Pixel standard deviation has been estimated from noise maps for BOOMERANG and *WMAP*. BOOMERANG standard deviation also takes into account calibration errors, which increase the flux error bars by ∼10%. In the case of *IRAS* and DIRBE we computed the rms of the data in several "clean" regions at high galactic latitudes and took the average standard deviation of the data as pixel error.

In Figure 2, the areas that we have identified as cirrus clouds are circled, and the approximate coordinates of the centers, as well as the cirrus areas, fluxes and column densities, are reported in Table 2. The hydrogen column densities have been measured using the Leiden/Argentine/Bonn (LAB) survey (Kalberla et al. 2005; Arnal et al. 2000; Bajaja et al. 2005).

We compared the BOOMERANG fluxes to those predicted by the model 8 of FDS (Finkbeiner et al. 1999) at the nominal BOOMERANG frequencies, measuring the fluxes from extrapolated simulations of dust maps in the cloud regions we identified. A flux-to-flux comparison, made by plotting the real data fluxes versus the predicted ones, has a best-fit line with slopes 1.5 ± 0.3 and 0.9 ± 0.3 at 345 and 245 GHz, respectively.

3.1. Estimation of Cirrus Physical Parameters

It is generally accepted that the submillimeter spectrum of thermal dust can be expressed as a blackbody times a frequency dependent (power-law) emissivity factor. Simple emission models predict the emissivity factor to be approximately 2. Significant variations to the $\beta = 2$ emissivity law occur when taking into account the disordered structure of amorphous dust grains (Meny et al. 2007). At tens of arcminutes angular scales, it is also possible to detect different temperatures in the structures due to different dust components as for example in model 8 of Finkbeiner et al. (1999). In these cases, an isothermal model could lead to spectral index values smaller than 2 while a two temperatures model with a cold dust component at approximately 10 K and $\beta = 2$ could better approximate the physics of the emission. Both these models are tested on our sample.

In order to analyze cirrus characteristics (e.g., temperature and emissivity) we fit the flux data taking into account two contributions: a blackbody times a frequency-dependent emissivity emission component, peaking in the far infra-red region, and a second emission component at lower frequencies parameterized as a power law with a spectral index able to reproduce synchrotron or free–free emission. When assuming the thermal dust emission to be isothermal, the spectral energy distribution

Table 2
Cloud Locations and Measured Flux

Region	1	2	3	4	5	6	7	8
R.A. (deg)	84.7	88.4	80.5	83.3	87.0	80.0	78.5	84.5
Decl. (deg)	−48.3	−48.1	−45.5	−43.0	−40.5	−49.0	−42.0	−49.5
Area (deg^2)	0.4	5.8	8.0	2.7	5.6	6.0	2.5	0.5
S_K (Jy)	< 0.1	< 0.1	3.7 ± 0.4	< 0.1	0.7 ± 0.1	< 0.2	< 0.2	< 0.2
S_{Ka} (Jy)	< 0.2	< 0.2	2.1 ± 0.2	< 0.1	0.8 ± 0.2	< 0.2	< 0.3	< 0.2
S_Q (Jy)	< 0.3	< 0.4	1.1 ± 0.2	0.2 ± 0.1	0.8 ± 0.2	< 0.3	< 0.4	< 0.6
S_V (Jy)	< 0.5	< 0.6	< 0.5	< 0.7	1.7 ± 0.7	< 0.9	< 0.7	< 0.7
S_W (Jy)	< 1.0	< 1.0	< 1.0	< 1.1	1.7 ± 1.3	< 1.3	< 1.0	< 1.1
S_{B245} (Jy)	< 2	14 ± 5	8 ± 4	3 ± 2	7 ± 6	26 ± 12	6 ± 2	0.6 ± 0.4
S_{B345} (Jy)	5 ± 1	83 ± 33	90 ± 33	7 ± 2	74 ± 20	90 ± 32	22 ± 8	3.5 ± 1.6
S_{D240} (Jy)	81 ± 30	778 ± 385	500 ± 354	384 ± 175	686 ± 224	430 ± 345	187 ± 81	72 ± 29
S_{I100} (Jy)	44.2 ± 5.3	560 ± 102	585 ± 151	185 ± 25	446 ± 86	305 ± 95	99 ± 16	< 8
N(HI) $(10^{21}\,{\rm cm}^{-2})$	0.375	0.622	0.374	0.433	0.441	0.222	0.323	0.331

Notes. Coordinates of the centers and areas of circled regions in Figures 1 and 2 (second, third, and fourth rows, respectively). The following rows report flux values registered by 5 yr *WMAP*, BOOMERANG, D240, and I100 channels corrected from the bias with the procedure described in Section 3.1. In the last row corresponding HI column densities are reported.

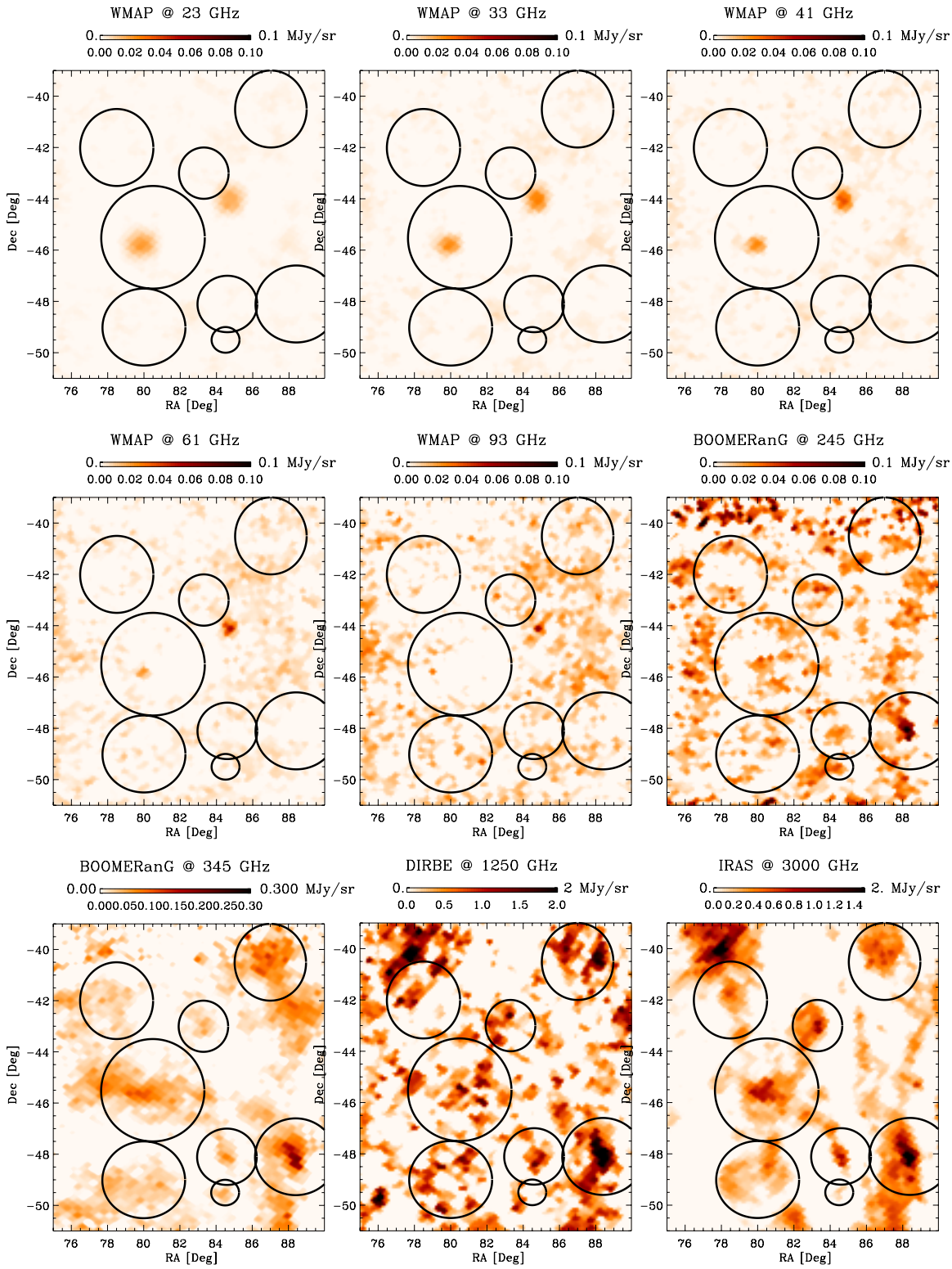

Figure 2. BOOMERANG deep region observed, from top to bottom and from left to right, by *WMAP* at 23, 33, 41, 61, and 93 GHz, by BOOMERANG at 245 GHz and 345 GHz, by DIRBE at 240 μm, and by *IRAS* at 100 μm.

(A color version of this figure is available in the online journal.)

(SED) results in

$$S(\nu) = A_1 \left(\frac{\nu}{\nu_0}\right)^{\alpha} + A_2 \left(\frac{\nu}{\nu_1}\right)^{\beta} \mathrm{bb}(\nu, T_d), \qquad (4)$$

where $\mathrm{bb}(\nu, T_d)$ is the standard blackbody function. ν_0 and ν_1 are 33 GHz and 3000 GHz, respectively. T_d is the temperature of the considered dust cloud, β is the corresponding spectral index, and α is the spectral index of the low frequencies contribution. A_1 and A_2 represent the amplitude of the two components, which at these galactic latitudes is proportional to the optical depth. When modeling the thermal dust emission with a warm and a cold

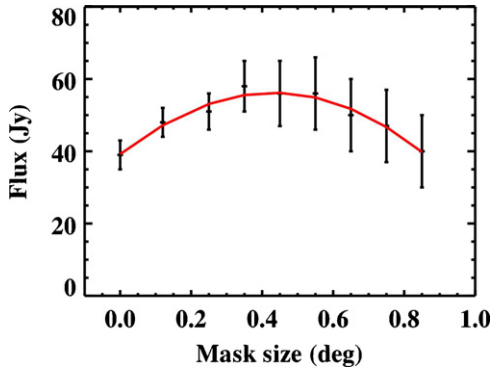

Figure 3. Plot of the integrated flux vs. size of the integration area for cirrus 2 at 345 GHz. The initial region, corresponding to 0.°0, is selected using the correlation map (Figure 1) and then increased with the technique described in the text in order to preserve the shape of the cloud. The solid line is the best Gaussian fit on the estimated fluxes. In this case, the maximum flux is found in a mask increased of 0.°45 with respect to the starting one. The final value of the flux and associated error are those measured with this mask size.

(A color version of this figure is available in the online journal.)

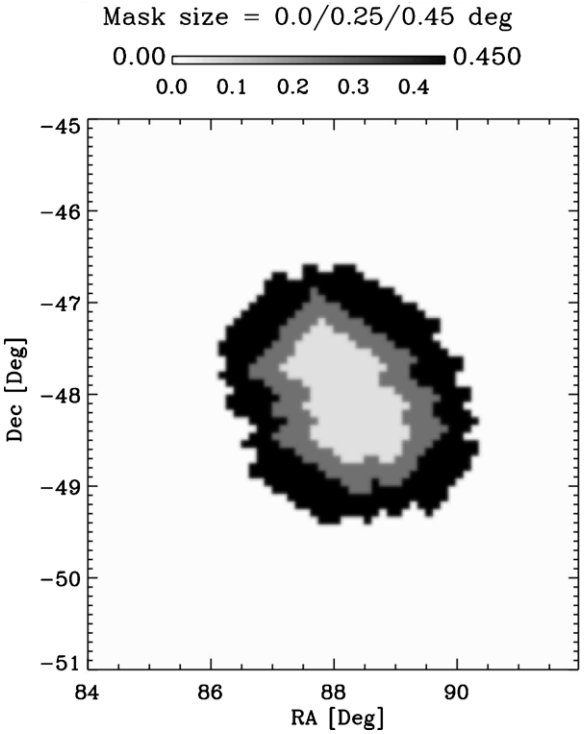

Figure 4. Starting mask (inner contour) and 0.°25 and 0.°45 "radius" mask (medium and outer contour respectively), the latter corresponding to maximum integrated flux, for cirrus 2 at 345 GHz (same as in Figure 3).

component we set the spectral index of both to the theoretical value of 2 and the SED becomes

$$S_2(\nu) = B_1 \left(\frac{\nu}{\nu_0}\right)^{\alpha_2} + B_2 \left(\frac{\nu}{\nu_1}\right)^2 \mathrm{bb}(\nu, T_w) + B_3 \left(\frac{\nu}{\nu_1}\right)^2 \mathrm{bb}(\nu, T_c), \quad (5)$$

where T_c and T_w are the temperatures of the cold and warm components, respectively, and B_2 and B_3 the corresponding amplitudes. T_c is set to 10 K while T_w varies. B_1 and α_2 describe the amplitude and the emissivity of the low frequency component, respectively.

Table 3
Priors

Parameter	Limits
α	Free
T_d	0–40
T_w	0–40
β	−1 to 10.0
A_1	> 0
A_2	> 0
α_2	Free
B_1	> 0
B_2	> 0
B_3	> 0

Notes. List of a priori probability density imposed on parameter set.

From the measured SED we estimate the parameters A_1, A_2, α, β, and T_d in the isothermal model, and the parameters B_1, B_2, B_3, T_w, α_2 in the two components model, using a Monte Carlo Markov Chain (MCMC) algorithm (Christensen et al. 2001; Lewis & Bridle 2002). Following Bayesian statistics, the probability to have a set of parameters $\mathbf{p}$ given a set of data $\mathbf{d}$ is

$$P(\mathbf{p}|\mathbf{d}) \propto P(\mathbf{p})P(\mathbf{d}|\mathbf{p}), \quad (6)$$

where $P(\mathbf{p})$ is the a priori probability density of the parameters set $\mathbf{p}$ and $P(\mathbf{d}|\mathbf{p})$ is the probability density of data $\mathbf{d}$ given a set of parameters $\mathbf{p}$, named the likelihood function. The posterior probability $P(\mathbf{p}|\mathbf{d})$ is estimated using MCMC algorithm. Given a set $\mathbf{p}_i$, with likelihood L_i and posterior probability $P(\mathbf{p}_i|\mathbf{d})$, the MCMC algorithm generates an independent set $\mathbf{p}_{i+1}$ with likelihood L_{i+1} and posterior probability $P(\mathbf{p}_{i+1}|\mathbf{d})$. This second set is accepted according to a rule which also guarantees a good sampling of the probability density in a reasonable computational time. For example in the Metropolis–Hastings algorithm the new set $\mathbf{p}_{i+1}$ is always accepted if

$$\Lambda(i+1, i) = \frac{P(\mathbf{p}_{i+1}|\mathbf{d})}{P(\mathbf{p}_i|\mathbf{d})} = \frac{L_{i+1}P(\mathbf{p}_{i+1})}{L_i P(\mathbf{p}_i)} > 1. \quad (7)$$

This guarantees the convergence to the maximum of the likelihood function. If instead $\Lambda(i+1, i) < 1$, the new set is accepted with a probability proportional to the ratio $\Lambda(i+1, i)$. This ensures a good sampling of the distribution. For a better description of the operation of the algorithm see Christensen et al. (2001) and Lewis & Bridle (2002). We chose wide flat a priori probability densities of the parameters, as reported in Table 3. Three chains for each cloud have been run, starting from different points of the parameter space. The convergence has been checked using the test algorithm encoded in the GetDist software, available in the public CosmoMC package.[22]

The combination of the BOOMERANG scanning strategy and AC coupling induces an effective filtering to the sky signal. To take the induced bias into account, we applied the same effective filtering to all the other data sets as described in Section 2, and estimated its effect by means of simulations. Since filtering effects depend strongly on the scanning strategy, which translates in the map into a dependence on the position of the cloud and on the nearby structures, we produced for each cirrus cloud 100 simulations with the same shape, position and noise properties of the measured cloud, and processed each

[22] http://cosmologist.info/cosmomc/

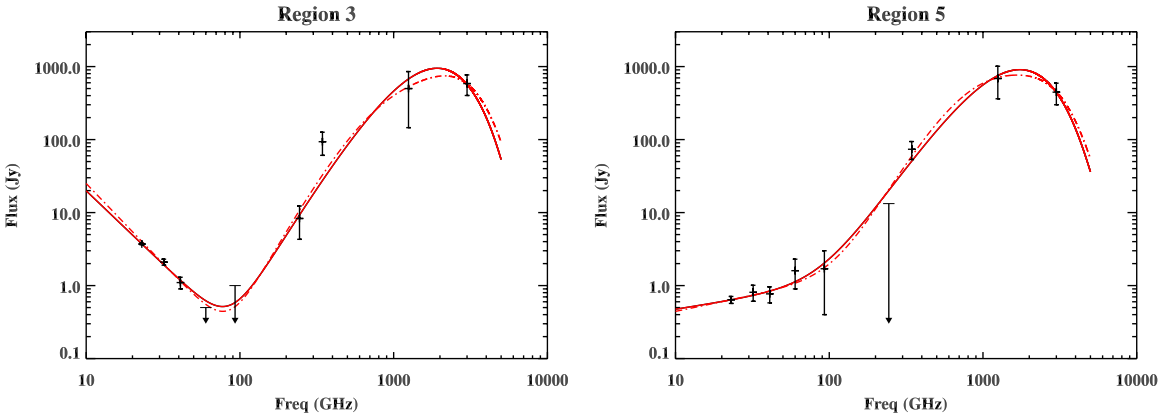

Figure 5. Spectra of four cirrus clouds from 23 to 3000 GHz (13 mm to 100 μm in wavelength). Solid line: fitting curve of Equation (4). Dashed line: fitting curve of Equation (5). Low frequency emission is detectable and is fitted by means of a frequency-dependent power law.
(A color version of this figure is available in the online journal.)

Table 4
Physical Characteristics for Each Dust Structure in the Isothermal Model

Region	α	T_d (K)	β	log A_1	log A_2	$P(S)$
1	···	17.0 ± 2.3	1.8 ± 0.3	< -1.5	-2.2 ± 0.4	0.52
2	···	16.9 ± 2.8	1.8 ± 0.4	< 0.1	-1.2 ± 0.5	0.79
3	-2.0 ± 0.2	20.4 ± 5.4	1.5 ± 0.5	0.3 ± 0.1	-1.9 ± 0.6	0.71
4	···	15.1 ± 1.2	2.6 ± 0.3	< 1.6	-1.2 ± 0.3	0.53
5	0.4 ± 0.3	19.0 ± 2.8	1.4 ± 0.3	-1.4 ± 0.2	-1.7 ± 0.4	0.69
6	···	18.0 ± 3.9	1.3 ± 0.3	< -1.8	-1.6 ± 0.5	0.91
7	···	19.6 ± 4.1	1.1 ± 0.5	< -0.2	-2.4 ± 0.5	0.47
8	···	6.5 ± 2.6	5.1 ± 1.8	< -3.5	1.7 ± 1.3	0.56

Notes. Physical parameters of the clouds assuming an isothermal (Equation (4)) model of dust emission, as measured using an MCMC algorithm. The errors correspond to 68% confidence interval.

simulation through the pipeline applied to the data. Comparing the average output flux values with the input ones we obtain the bias factors the measured fluxes have to be corrected for. The factors show that approximately 20% of the sky signal is dumped by the pipeline. As expected, these factors depend on the dilution of the cirrus in the beam and on position and shape of the cloud itself.

4. RESULTS

Our analysis shows that the two temperatures model of Equation (5) and the isothermal model of Equation (4) are statistically equivalent. However, the 10 K component is poorly constrained in almost all clouds, as its amplitude B_3 is consistent with zero. The temperature of the warm component T_w is consistent with the temperature T_d estimated with the isothermal fit. This consistency provides a further check on the temperature values obtained.

We can distinguish two sets of cirrus clouds: the first consists of two of the eight selected dust regions (marked with numbers 3 and 5 in Figure 1) whose emission is clearly detected in the full range of analyzed frequencies; we are then able to derive both the thermal dust and low frequency component. The SED for these clouds, estimated with both the isothermal and the two-temperatures model, is shown in Figure 5. The remaining six clouds (numbers 1, 2, 4, 6, 7, and 8) form the second set and present the thermal dust component only, as plotted in Figure 6. This can be seen in the values of the parameter A_1, and consequently of the spectral index α, which in the second set are un-determined.

The characteristics of each cloud for the isothermal and the two temperatures model are reported in Tables 4 and 5, respectively. In order to check the goodness of the fit, the last columns of these tables report the cumulative distribution function P of a χ^2 distribution with the proper number of degrees of freedom. The ideal fit should have $P \sim 0.5$; $P \ll 0.5$ is an indication of overestimated error bars; $P \gg 0.5$ indicates that the fitting function is not a good model.

One- and two-dimensional posterior probability of parameters in Equation (4) are shown for the cloud number 3, as example, in Figure 7.

Assuming an isothermal model of dust emission the clouds have dust temperatures in the range $T_{\rm d} \in [6; 21]$ K, and emissivities $\beta \in [1.1; 5]$. The amplitude and spectral index of the warm dust and the low frequency component estimated using the two components model are fully consistent with the correspondent values estimated with the isothermal model.

In order to study dust emissivity variation across the patch and its dependence on dust temperature, in the following analysis we will refer only to the isothermal model for the dust emission.

4.1. Temperature Dependence of the Spectral Index

Dust emissivities and temperatures in the BOOMERANG deep field cover a range of values (see Table 4). The spectral shape of the thermal component of the dust emissivity (second term of Equation (4)) is strongly dependent on a combination of $T_{\rm d}$ and β, whose two-dimensional posterior probability has a elongated, slant shape (Figure 7), indicating a degeneracy between these two parameters. Two more degeneracy figures

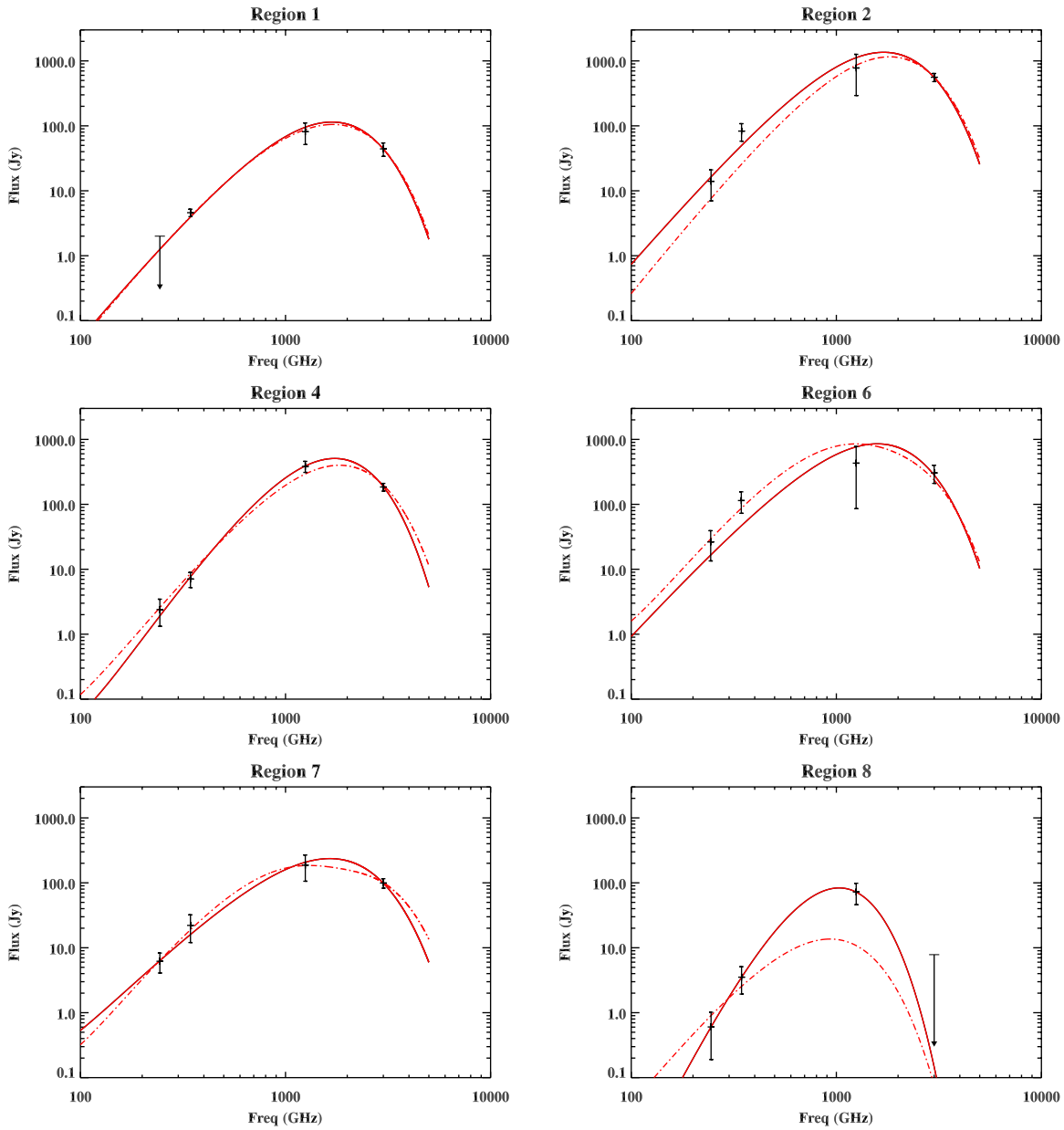

Figure 6. SEDs of three cirrus clouds from 245 to 3000 GHz (1.2 mm to 100 μm in wavelength). Solid line: fitting curve of Equation (4). Dashed line: fitting curve of Equation (5). These sources do not have a significant low frequency emission so only the thermal dust emission is shown.
(A color version of this figure is available in the online journal.)

Table 5
Physical Characteristics for Each Dust Structure in the Two-component Model

Region	α_2	T_w (K)	log B_1	log B_2	log B_3	$P(S_2)$
1	···	17.1 ± 2.6	< -4	-2.3 ± 0.4	< -2	0.62
2	···	18.7 ± 4.7	< 0.1	-1.6 ± 0.6	< -0.8	0.82
3	-2.2 ± 0.2	21.8 ± 5.4	0.3 ± 0.1	-2.0 ± 0.6	< -0.9	0.65
4	···	17.7 ± 0.5	0.3 ± 0.1	-1.7 ± 0.1	< -4.5	0.56
5	0.4 ± 0.2	20.3 ± 5.5	-0.2 ± 0.1	-1.8 ± 0.7	< -0.6	0.68
6	···	17.6 ± 4.5	< -0.4	-1.7 ± 0.8	-0.4 ± 0.3	0.76
7	···	21.1 ± 3.1	< -0.2	-2.7 ± 0.7	-1.0 ± 0.4	0.38
8	···	9.0 ± 2.1	< -2.3	-1.7 ± 0.7	< -0.1	0.62

Notes. Physical parameters of the clouds assuming a two-component (Equation (5)) model of dust emission. The errors correspond to the 68% confidence interval. The amplitude and spectral index of the low frequency component and of the warm dust component are fully consistent with the ones estimated using the isothermal model. The cold component described by the coefficient B_3 is determined in two clouds.

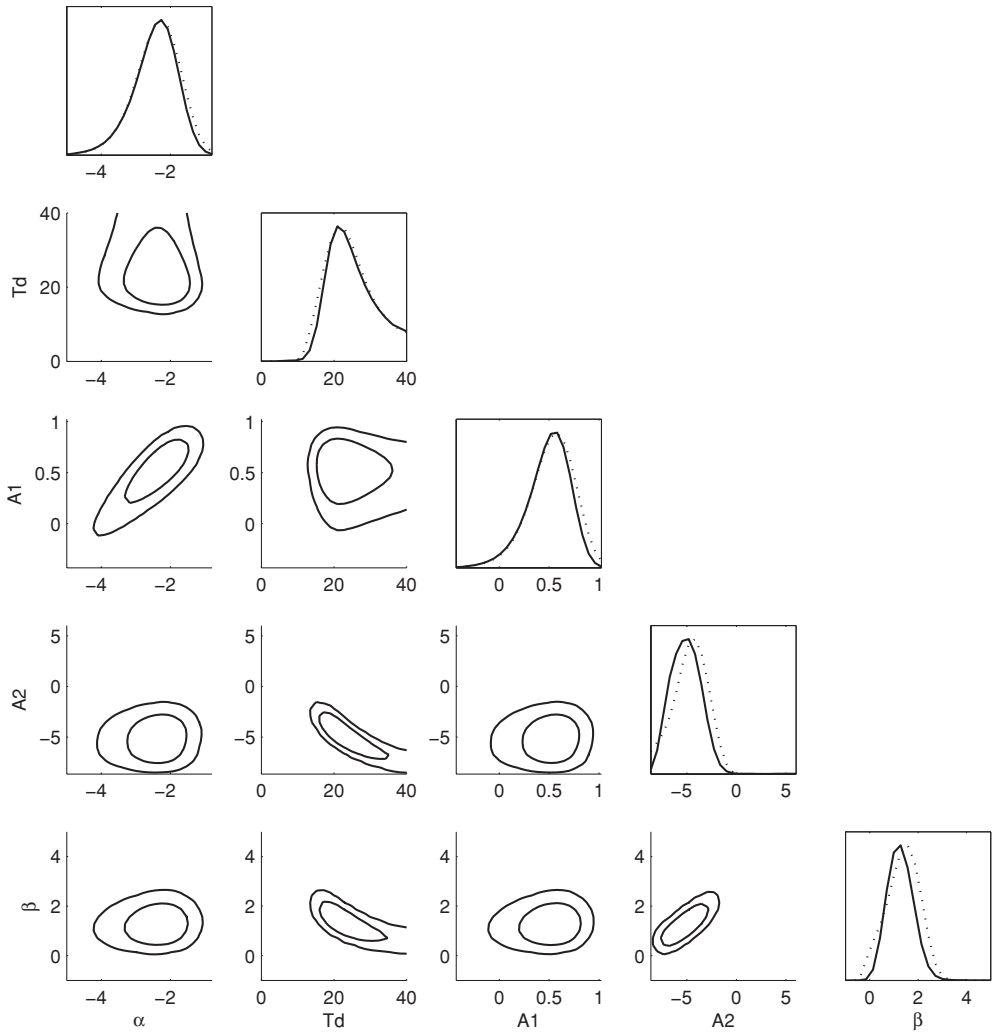

Figure 7. One- and two-dimensional posterior probability of the parameters for one of the clouds. The posterior probability is obtained using an MCMC algorithm. The black ellipses show the 68% and 95% confidence levels. In this case we consider region 3, and parameters values are $\alpha = -2.0 \pm 0.2$, $T_d = 20.4 \pm 5.4$, $\beta = 1.5 \pm 0.5$, $\log(A_1) = 0.3 \pm 0.1$, and $\log(A_2) = -1.9 \pm 0.6$.

are obtained in the A_2–β and A_1–α planes, as expected from the functional form. Previous works on Pronaos (Dupac et al. 2003) and Archeops (Désert et al. 2008) data which analyze many cold clouds find an inverse relation between the dust temperature and its spectral index, the former being expressed as a function of the latter.

Given the shape of the posterior probability we find in our data, we want to investigate whether in our case the β–$T_{\rm d}$ relation is a physical characteristic of the dust or just a consequence of the functional form and of measurements errors. We run then an MCMC on each region expressing, in Equation (4), β as a function of T_d following the two models:

1. Désert et al. (2008), defined by the relation

$$\beta = A \times T_d^{\rho}; \tag{8}$$

2. Dupac et al. (2003), through the relation

$$\beta = \frac{1}{\delta + \omega T_d}, \tag{9}$$

where $A = 11.5 \pm 3.8$, $\rho = -0.66 \pm 0.05$, $\delta = 0.40 \pm 0.02$, $\omega = 0.0079 \pm 0.0005\,{\rm K}^{-1}$ are the values derived from the Archeops and Pronaos data, respectively.

In order to check the concordance between BOOMERANG and the other considered experiments, we fit our sample using the two models quoted before (Equations (7) and (8)) including the error induced by the degeneracy shape relation. We thus perform the fit on eight random points, one for each cirrus, within the 68% contour of the two-dimensional posterior probabilities. We repeat this procedure 60,000 times for each model, a number of steps which allows a good sampling of the distributions of the parameters A, ρ, δ, and ω in Equations (7) and (8), respectively. This technique allows a complete sampling of the degeneracy, not dominated by its shape in the final result. From the peaks and the standard deviations of the distributions we derive as best fits:

$$\beta = (33.3 \pm 6.0) \times {T_d}^{-1.1 \pm 0.1} \qquad \text{model 1}$$

$$\beta = \frac{1}{(0.035 \pm 0.004) \times T_d - (0.013 \pm 0.030)} \qquad \text{model 2}$$

finding a trend similar to the Archeops result. Figure 8 shows the points within the posterior probabilities 68% contour plot in the T_d–β plane, for all the analyzed structures together. The contours are also shown in solid lines. The dashed and solid lines show BOOMERANG parameters using models 1 and 2, respectively. The dotted and dash-dotted lines mark the best fits obtained by Archeops and Pronaos experiments, respectively.

Table 6
Free–Free and Synchrotron Contributions

Region #	$S_{ff}(Jy)$					$S_s(Jy)$				
	K	*Ka*	*Q*	*V*	*W*	*K*	*Ka*	*Q*	*V*	*W*
3	< 0.1	< 0.1	< 0.1	< 0.1	< 0.1	< 2.1	< 0.9	< 0.4	< 0.1	< 0.1
5	< 0.2	< 0.1	< 0.1	< 0.1	< 0.1	< 0.3	< 0.4	< 0.2	< 0.1	< 0.1

Notes. Upper limits on free–free and synchrotron emission in *WMAP* bands, estimated in regions that show a non-negligible flux at low frequency.

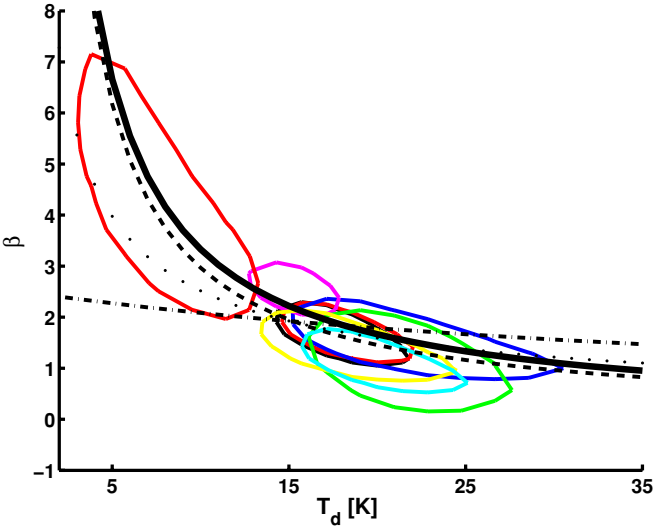

Figure 8. Two-dimensional $T_d - \beta$ posterior probability contour plot of the whole structures set. The contours are at 68% of confidence level; the points inside the contours are used for fitting Equations (7) and (8) as explained in the text. The solid and dashed lines show the BOOMERanG best fit following Désert et al. (2008) and Dupac et al. (2003) models, respectively. The dot and dot-dashed lines show the best fits from Archeops and Pronaos data sets, respectively.

(A color version of this figure is available in the online journal.)

4.2. Emission at Low Frequencies

As previously discussed, a low frequency emission is detected in regions 3 and 5. The spectral index α obtained from the fit of the flux in Jy can be converted in the corresponding spectral index γ in antenna temperature by the relation $\gamma = \alpha - 2$.

α is the spectral index reported in the second column of Table 4. According to this conversion we obtain $\gamma = -4.2 \pm 0.2$ in region 3 and $\gamma = -1.6 \pm 0.2$ in region 5. We expect the detected emission to be a combination of different emissions dominating in these bands, typically free–free and synchrotron with their typical power laws. Since the considered frequency range is limited we approximate the combination of the two emissions with a single power law. We also estimate the contribution of these components including the Hα SHASSA (The Southern Hα Sky Survey Atlas)[23] survey (Finkbeiner 2003) as monitor of free–free emission and the Haslam 408 MHz survey (Haslam et al. 1982) as monitor of synchrotron emission. Estimated fluxes are reported in Table 6; these values have to be considered as upper limits on the emission. Galactic free–free is negligible in both regions while synchrotron is dominant.

[23] http://amundsen.swarthmore.edu/

4.3. Spinning Dust

There has been recent interest in spinning dust emission both theoretically (Draine & Lazarian 1998) and observationally (e.g., de Oliveira-Costa et al. 2008; Gold et al. 2009). Large dust grains in cirrus clouds have a thermal emission which peaks at $\sim$250 μm, but smaller grains emit transiently at higher frequencies, and could also produce rotational emission by spinning at microwave frequencies. This could be relevant below 60 GHz.

The only regions showing a non-negligible low frequency emission are 3 and 5. Region 3 includes a radio source that dominates the signal at low frequency so we do not expect to find a significant spinning dust detection. In order to check whether signal in region 5 can be generated by rotational dust we have to remove free–free and synchrotron contributions, reported in Table 6, from the measured fluxes before estimating the spinning dust level. After the removal, no detection is found in that cloud either.

5. CONCLUSIONS

This paper analyzes the properties of galactic cirrus clouds at high latitude combining the high-frequency BOOMERanG data set together with *IRAS*, DIRBE and *WMAP*. We located eight clouds in the deep survey area of BOOMERanG and for each of them we estimated dust temperature and emissivity spectral index finding the temperature to be in the 7–20 K range and its emissivity spectral index in the 1–5 range. We also investigated the possibility of a two temperatures model to describe the dust emission, having both the components $\beta = 2$ and the cold component temperature $T_c = 10$ K. Within this model the temperature of the warm component is consistent with the temperature estimated using the isothermal model within 1σ error bars while the cold component is detected in regions 6 and 7. This, and the presence of a 6.5 K region, shows the presence of cold dust at high latitudes.

Taking into consideration the shape of the joint posterior probability of the parameters estimated with the isothermal model for each observed object, our data confirm a model in which temperature and spectral index are inversely correlated, as was suggested in previous analyses on Pronaos (Dupac et al. 2003) and Archeops (Désert et al. 2008) data.

A comparison to the extrapolation of *IRAS* data from Finkbeiner et al. (1999) indicates that this prediction has limited accuracy in the range of frequencies observed with BOOMERanG. In particular, the model seems to underestimate the dust brightness at 345 GHz by a factor of $\sim$1.5, being the equality with the model within 2σ.

At lower frequencies we detect a signal in the observed regions which is mostly generated by synchrotron and free–free. We do not find any evidence of spinning dust.

From this analysis it is clear that new data are required to improve the knowledge of properties of high galactic latitude cirrus clouds, and of dust in general. The method developed in this paper allows us to identify the location and shape of dust clouds, and to extract the flux from observations with different instruments at different wavelengths and angular resolutions. This technique can be proficiently used to analyze the forthcoming Planck and Herschel data sets, which will provide higher sensitivity, wider spectral range and, in the case of Planck, full sky coverage.

The authors acknowledge Jean-Philippe Bernard, Robert Crittenden, Alessandro Melchiorri and Max Tegmark for useful discussions. M.V. acknowledges support from the Faculty of the European Space Astronomy Center (ESAC-ESA). This activity has been supported by Italian Space Agency contracts COFIS, BOOMERANG and HiGal (I/038/08/0). We are grateful to the referee for helpful comments.

REFERENCES

Arendt, R. G., et al. 1998, ApJ, 508, 74
Arnal, E. M., Bajaja, E., Larrarte, J. J., Morras, R., & Pöppel, W. G. L. 2000, A&AS, 142, 35
Bajaja, E., Arnal, E. M., Larrarte, J. J., Morras, R., Pöppel, W. G. L., & Kalberla, P. M. W. 2005, A&A, 440, 767
Boggess, N. W., et al. 1992, ApJ, 397, 420
Bot, C., Helou, G., Boulanger, F., Lagache, G., Miville-Deschenes, M.-A., Draine, B., & Martin, P. 2009, ApJ, 695, 469
Boulanger, F., Abergel, A., Bernard, J., Burton, W. B., Desert, F., Hartmann, D., Lagache, G., & Puget, J. 1996, A&A, 312, 256
Christensen, N., Meyer, R., Knox, L., & Luey, B. 2001, Class. Quantum Grav., 18, 2677
Crill, B. P., et al. 2003, ApJS, 148, 527
de Gasperis, G., Balbi, A., Cabella, P., Natoli, P., & Vittorio, N. 2005, A&A, 436, 1159
de Oliveira-Costa, A., Tegmark, M., Gaensler, B. M., Jonas, J., Landecker, T. L., & Reich, P. 2008, MNRAS, 388, 247
De Troia, G., et al. 2007, ApJ, 670, L73
Désert, F.-X., et al. 2008, A&A, 481, 411
Draine, B. T., & Lazarian, A. 1998, ApJ, 508, 157
Dupac, X., et al. 2003, A&A, 404, L11
Finkbeiner, D. P. 2003, ApJS, 146, 407
Finkbeiner, D. P., Davis, M., & Schlegel, D. J. 1999, ApJ, 524, 867
Gold, B., et al. 2009, ApJS, 180, 265
Górski, K. M., Hivon, E., Banday, A. J., Wandelt, B. D., Hansen, F. K., Reinecke, M., & Bartelmann, M. 2005, ApJ, 622, 759
Haslam, C. G. T., Salter, C. J., Stoffel, H., & Wilson, W. E. 1982, A&AS, 47, 1
Hinshaw, G., et al. 2007, ApJS, 170, 288
Jones, W. C., et al. 2006, ApJ, 647, 823
Kalberla, P. M. W., Burton, W. B., Hartmann, D., Arnal, E. M., Bajaja, E., Morras, R., & Pöppel, W. G. L. 2005, A&A, 440, 775
Kiss, C., Ábrahám, P., Laureijs, R. J., Moór, A., & Birkmann, S. M. 2006, MNRAS, 373, 1213
Lagache, G., Abergel, A., Boulanger, F., & Puget, J.-L. 1998, A&A, 333, 709
Leach, S. M., et al. 2008, A&A, 491, 597
Lewis, A., & Bridle, S. 2002, Phys. Rev. D, 66, 103511
Low, F. J., Neugebauer, G., Gautier, III, T. N., & Gillett, F. 1984, BAAS, 16, 968
MacTavish, C. J., et al. 2006, ApJ, 647, 799
Masi, S., et al. 2001, ApJ, 553, L93
Masi, S., et al. 2006, A&A, 458, 687
Mather, J. C., et al. 1994, ApJ, 420, 439
Meny, C., Gromov, V., Boudet, N., Bernard, J.-P., Paradis, D., & Nayral, C. 2007, A&A, 468, 171
Miville-Deschênes, M.-A., & Lagache, G. 2005, ApJS, 157, 302
Montroy, T. E., et al. 2006, ApJ, 647, 813
Natoli, P., et al. 2009, arXiv:0905.4301
Netterfield, C. B., et al. 2009, ApJ, 707, 1824
Neugebauer, G., et al. 1984, ApJ, 278, L1
Pascale, E., et al. 2008, ApJ, 681, 400
Piacentini, F., et al. 2006, ApJ, 647, 833
Veneziani, M., et al. 2009, ApJ, 702, L61